Improving the frequency stability of capacitive ring-based Coriolis Vibrating Gyroscopes

Journal of Physics: Conference Series **2909** (2024) 012021 doi:10.1088/1742-6596/2909/1/012021

Improving the frequency stability of capacitive ring-based Coriolis Vibrating Gyroscopes

D. Arifin and S. McWilliam

Faculty of Engineering, University of Nottingham, UK

E-mail: davin.arifin2@nottingham.ac.uk

Abstract. MEMS capacitively operated ring-based Coriolis vibratory gyroscopes are used to measure angular rate. Under standard operating conditions the ring is driven into resonance and Coriolis coupling generates a response that is proportional to the applied angular rate. In practice capacitive devices are susceptible to electrostatic nonlinearities due to narrow capacitive gaps which potentially degrades the quality of the measurement. One issue is that large amplitude drive responses yield multi-harmonic response which distorts the sense output causing the rate output to vary periodically (i.e. frequency instability). In this research it is shown that this frequency instability can be negated relatively easily by incorporating additional harmonics in the drive force. To implement such an approach it is necessary to use a voltage distribution to generate the appropriate electrostatic forces to eliminate or reduce the multi-frequency mechanical response of the ring. A mathematical model is used to quantify the effects of the implementation of the voltage distribution in terms of discrete Fourier transform of the ring response and the calculated Allan deviation. It is shown that the proposed implementation approximates linear behaviour by reducing the multi-harmonic response by orders of magnitude.

1. Introduction

MEMS ring-based Coriolis Vibratory Gyroscopes (CVG's) are conventionally operated within linear operating regimes where the operational drive and sense modes are linearly coupled by the Coriolis force in the presence of an angular rate [1]. The sense displacement amplitude is proportional to the angular rate, which is a key feature enabling the device to operate as an angular rate sensor. Within the linear operating regime, standard CVG operation involves the sense mode vibration exhibiting the following important characteristics. First, the angular rate sensitivity of the sense displacement amplitude scales proportionally with the drive displacement amplitude. As such, implementing larger drive displacement amplitudes is conventionally desirable to maximize the quality of the device rate output through signal-to-noise ratio (SNR) enhancements [2]. Second, the sense mode vibrates in phase/antiphase relative to the drive mode, resulting in zero quadrature sense displacement component due to the degeneracy of the ring flexural modes [3].

MEMS ring-based CVG's are commonly operated capacitively due to compatibility with most microfabrication processes [1]. However, the electrostatic forces in capacitive MEMS CVG's are known to be nonlinear [4-7]. The electrostatic nonlinearities are particularly strong for these miniaturized devices due to the narrow capacitive gaps between the ring and electrodes. Electrostatic nonlinearities cause the dynamics of the drive and sense modes to deviate from the previously discussed characteristics expected in standard linear device operation [4]. As such, electrostatic nonlinearities are commonly

regarded as undesirable effects at larger drive displacement amplitudes, hindering attained rate sensitivity amplification at such operating regimes [7].

Frequency instability in mechanical resonators has been reported as a potential nonlinearity-induced performance degradation [6, 8, 9], in which the oscillation frequency of the resonator fluctuates with time, causing phase distortions. These distortions accumulate over time causing the oscillator phase to diffuse [10]. In the context of CVG's, the drive frequency fluctuations have significant implications on the output of the device [11], as the rate and quadrature outputs are conventionally obtained via demodulation relative to the drive displacement phase [11, 12]. An approach involving exploiting internal resonance between two distinct modes to improve the frequency stability in mechanical resonators has been reported, relying on the mechanical energy exchange between the modes involved to oppose random perturbations imposed on the oscillation frequency [13]. This approach is demonstrated for a system where the two modes have differing nonlinearity types, i.e. hardening or softening. Another approach involves operating the resonator at the zero dispersion point [8], where the frequency is locally insensitive to vibration amplitude fluctuations. A key requirement of this implementation is a differing nonlinearity type between the cubic and quantic-ordered stiffnesses, which is unlikely the case in capacitive ring-based CVG's due to the dominance of the softening electrostatic nonlinearities. It has also been shown that frequency stability can be improved through the use of a phase shifter, which uses the phase of the response as a control parameter to fixate the frequency [14-16]. In most of these studies, the frequency fluctuations are described as a result of random amplitude noise due to the amplitude-frequency coupling inherent in nonlinear systems. Deterministic sources of such effects, however, have not been widely reported or investigated.

This research focuses on addressing the multi-frequency ring vibrations as a source of the frequency instability in MEMS CVG's. This multi-frequency behaviour is a deterministic trait of nonlinear systems [17, 18] and may influence the capacitive sense output due to the nonlinear relationship between capacitance variation and mechanical displacement [1, 2]. The research aims to improve frequency stability by reducing or eliminating this multi-frequency behaviour. The paper is structured as follows. The fundamental mechanisms of the proposed approach are first described in Section 2. Using a simplified case as a starting point, the required force conditions to eliminate multi-frequency response are identified. In Section 3. the device considered is described, including the form of the voltage distribution applied to each electrode to apply the force condition identified in Section 2. In Section 4. the proposed forcing approach is implemented on the coupled drive and sense dynamics. Equations of motion are developed and analysed to identify the voltage conditions necessary to achieve the force condition identified in Section 2. The effectiveness of the proposed implementation is then assessed in Section 5. The modal amplitude spectra and Allan deviation of the rate output are considered and Finite element (FE) results are included to validate the theoretical analysis.

2. Proposed method

As a starting point, the basic form of the drive equation of motion in the presence of external electrostatic forces is stated. For simplicity, the drive mode is conventionally modelled as a single degree-of-freedom oscillator where Coriolis back coupling from the sense mode is neglected [1, 6, 19]. because in practice the sense response is much smaller than the drive response. In this case, the nonlinear drive response X_s is described by:

$$\ddot{X}_s + 2\Gamma\dot{X}_s + {\omega_s}^2 X_s + \gamma_s {X_s}^3 = \chi_s \cos\omega t + f_{s,b}(t) \quad (1)$$

In (1), subscript 's' denotes the basic, simplified form of the equation of motion. X_s is the drive mode displacement. Γ is the linear damping coefficient. ${\omega_s}^2$ and γ_s are the linear resonant frequency and Duffing coefficient respectively. $\chi_s \cos\omega t$ is the harmonic drive force which is used to initiate the drive mode vibration at frequency ω. $f_{s,b}(t)$ is an additional balancing force used to ensure single-frequency response, which is to be determined.

For the unbalanced case ($f_{s,b} = 0$) the steady-state response is multi-harmonic due to the nonlinear restoring force $\gamma_s {X_s}^3$ in (1), given by $X_s = \sum_{m=1}^{m_{max}} \{x^a_{s,2m-1} \cos[(2m-1)\omega t] - x^q_{s,2m-1} \sin[(2m-$

$1)\omega t]\}$, where m_{max} is the number of harmonics retained in the expression and $m = 1$ defines the fundamental frequency component. $x_{s,2m-1}^{i/a}$ and $x_{s,2m-1}^{q}$ are the phase-decomposed drive amplitudes, representing the in/antiphase and quadrature response components respectively. The complexity of solving for $x_{s,2m-1}^{i/a}$ and $x_{s,2m-1}^{q}$ increases with m_{max} and so the number of Fourier terms is chosen such that there are as many harmonic components as are necessary to achieve the desired accuracy [17].

In practice, the phase-lock loop (PLL) is used to ensure drive mode resonance [6]. The target single-frequency drive response in this implementation is $X_{s,t} = x_{s,1}^{q} \sin \omega t$ and substituting $X_{s,t} = x_{s,1}^{q} \sin \omega t$ in (1), and solving for $f_{s,b}(t)$ gives the following:

$$f_{s,b}(t) = f_{s,b}(t)|_t = -x_{s,1}^{q}\left(\omega^2 - {\omega_{s,X}}^2\right) \sin \omega t - \frac{1}{4}\gamma_s {x_{s,1}^{q}}^3 \sin 3\omega t \tag{2}$$

where ${\omega_{s,X}}^2 = {\omega_s}^2 + \frac{3}{4}\gamma_s {x_{s,1}^{q}}^2$ is the drive resonant frequency. When excitation frequency $\omega = \omega_{s,X}$, a residual force $-\frac{1}{4}\gamma_s {x_{s,1}^{q}}^3 \sin 3\omega t$ is present on the left side of (1). Using $f_{s,b}(t)$ to counterbalance this residual force using force condition (2) ensures that the targeted single-frequency drive response $X_{s,t} = x_{s,1}^{q} \sin \omega t$ is the exact solution of (1), eliminating the multi-frequency behaviour. Thus in addition to the harmonic drive force $\chi_s \cos \omega t$ applied, an additional force proportional to $\sin 3\omega t$ must be applied to counteract the Duffing nonlinearity. In practice, a control system can be used to adjust the amplitude of this force until condition in (2) is satisfied.

To demonstrate the impact of applying force (2), Figure 1 shows the amplitude spectra of the drive displacement obtained by solving (1) for the steady-state drive displacement for the cases $f_{s,b} = 0$ and $f_{s,b}(t) = f_{s,b}(t)|_t$. In both cases, the numerical values of the modal parameters are $\Gamma = 56.4$ Hz, $\omega_s = 11.4$ kHz, $\gamma_s = -4.3$ GHz^2/m^2, $\chi_s = 7.1$ N/kg, resulting in a resonant drive amplitude at $x_{s,1}^{q} = 0.14$ μm.

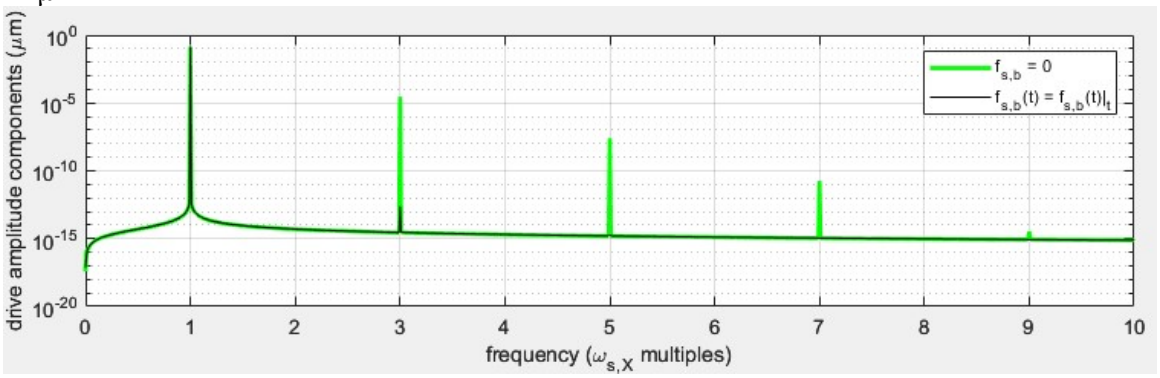

Figure 1. Drive amplitude spectra for balanced ($f_{s,b} = 0$) and unbalanced ($f_{s,b}(t) = f_{s,b}(t)|_t$) cases .

When $f_{s,b} = 0$ the drive displacement is composed of amplitude components at frequencies $\omega_{s,X}$, $3\omega_{s,X}$, $5\omega_{s,X}$, ⋯. The amplitude components decrease by orders of magnitude as the harmonic number increases due to the weak nonlinearity. However, when $f_{s,b}(t) = f_{s,b}(t)|_t$, the higher harmonic response components are significantly reduced when the residual forces from the Duffing nonlinearity are negated.

The approach outlined here can be extended to account for higher order nonlinearities. E.g. if a quantic restoring force proportional to ${X_s}^5$ is present in (1), substituting $X_{s,t} = x_{s,1}^{q} \sin \omega t$ indicates balancing force $f_{s,b}(t)$ must contain an additional force proportional to $\sin 5\omega t$. However, for simplicity, the following investigation only accounts for cubic-ordered electrostatic nonlinearities.

In what follows, electrostatic forces will be used to replicate the force condition described in this section.

3. Device and electrostatic configuration

Figure 2 shows the basic layout of the capacitive device considered including device dimensions and drive and sense deflections. 8 evenly distributed electrodes are implemented inside and outside the ring circumference to generate the required electrostatic forces to achieve the force condition described in Section 2. The use of 8 evenly distributed electrodes is the minimum number typically implemented in practice [20, 21].

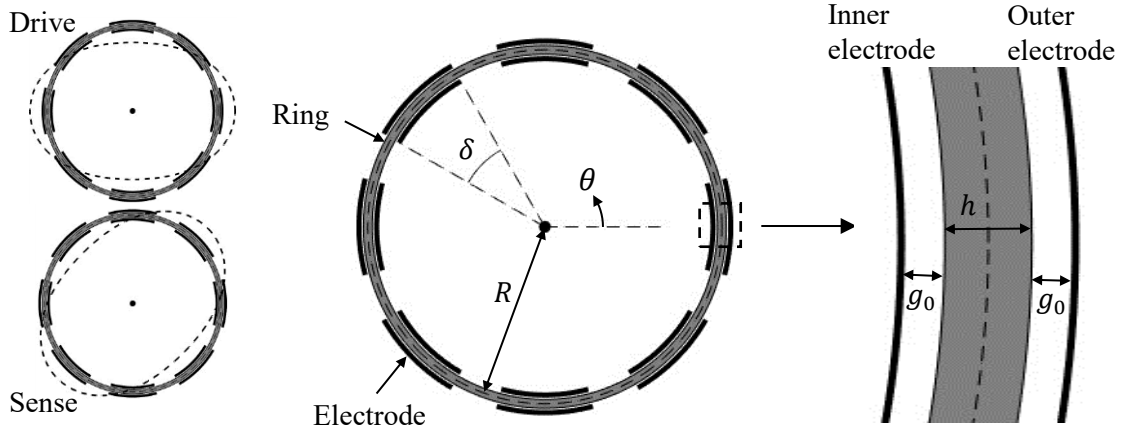

Figure 2. Device setup implementing 8 evenly distributed inner and outer electrodes and the resulting drive and sense mode deflection shapes.

Due to the miniature size of these devices, the capacitive gap g_0 is narrow, typically within the order of 1 or 10 μm and each ring-electrode pair approximates parallel-plate capacitors [5, 7, 19]. Electrostatic nonlinearity is significant when the flexural displacement amplitudes increase relative to the gap size, due to the nonlinear relationship between the capacitance and the displacement. This is a trade-off for improved measurement sensitivity when using variable-gap type capacitive devices [1].

The most basic form of voltage distribution applied to each electrode consists of bias and drive voltage components [19]. However, in this investigation the voltage distribution must generate additional electrostatic forces fulfilling the role of $f_{s,b}(t)$ in (1) for both the drive and sense modes. The chosen voltage distribution is described as a discrete Fourier series. Defining the mean angular position of the i^{th} inner/outer electrode (i is an integer ranging from 1 to 8) $\theta = \theta_0(i) = i\pi/4$, the voltages applied to the i^{th} electrodes are given by:

$$V^{\pm}(i) = V_0 \pm \left(V_{\text{AC}} \cos \omega t + V_{X,3\omega} \sin 3\omega t\right) \cos 2\theta_0(i) \pm \left(V_{Y,\omega} \sin \omega t + V_{Y,3\omega} \sin 3\omega t\right) \sin 2\theta_0(i) \quad (3)$$

where $V^+(i)$ and $V^-(i)$ represent the voltage distributions corresponding to the outer and inner electrode sets respectively.

V_0 is the DC bias voltage component, which is typically the largest voltage component to maintain the polarity of the total voltage applied to each electrode. The bias voltage is uniformly applied to all electrodes, and so is the same for all electrodes.

V_{AC} defines the amplitude of the drive voltage component and ω is the drive resonance frequency. The drive voltage is characterized by a $\cos 2\theta_0(i)$ variation from electrode to electrode to generate the required 'push-pull' electrostatic forces for supporting the shape of the drive mode shown in Figure 2. The drive voltage applied to the inner and outer electrodes act in antiphase and accounts for the opposite changes in capacitance corresponding to the inner and outer electrodes as the ring vibrates.

$V_{Y,\omega}$ defines the amplitude of the sense balancing voltage component at frequency ω. This voltage component is used to nullify quadrature errors [22] by ensuring an in/antiphase relationship between the

drive and sense modes. This voltage component is characterised by a $\sin 2\theta_0(i)$ variation, which generates direct electrostatic forces on the sense mode similar to the drive voltage.

$V_{X,3\omega}$ and $V_{Y,3\omega}$ are the amplitudes of the drive and sense balancing voltage components respectively at frequency 3ω. These triple frequency balancing voltage components generate direct electrostatic forces on the drive and sense modes to negate the multi-frequency vibrational behaviour due to the electrostatic nonlinearities, using the concept discussed in Section 2. These voltages are characterised by a $\sin 3\omega t$ time variation, due to force condition (2).

The voltage distribution in (3) is used to determine the electrostatic potential energy [1], based on which expressions for the nonlinear electrostatic forces can be developed, and these forces are incorporated into the modal equations of motion, described next.

4. Implementation

In this section, the forcing concept in Section 2. is implemented on a typical mode-coupled gyroscope model to address multi-frequency behaviour and improve frequency stability. Nonlinear modal equations of motion are used to identify the voltage requirements to achieve the forcing condition in Section 2.

4.1. Equations of motion

The equations of motion are developed using Lagrange's equations, which has been widely implemented in the literature [5, 7, 19]. Expressions for the ring kinetic and bending potential energies, the total bending potential energy of the support beams and the energy dissipation rate and the electrostatic potential energy from the voltage distribution in (3) are obtained, subsequently giving the following form for the modal mass-normalised equations of motion:

$$\ddot{X} + 2\Gamma\dot{X} + \left(\omega_{\mathrm{m}}{}^2 - \omega_0{}^2 + \kappa_0 \frac{Y^2}{g_0{}^2}\right)X + \gamma_0 \frac{X^3}{g_0{}^2} = G_\Omega \Omega \dot{Y} + f_X(t) \tag{4a}$$

$$\ddot{Y} + 2\Gamma\dot{Y} + \left(\omega_{\mathrm{m}}{}^2 - \omega_0{}^2 + \kappa_0 \frac{X^2}{g_0{}^2}\right)Y + \gamma_0 \frac{Y^3}{g_0{}^2} = -G_\Omega \Omega \dot{X} + f_Y(t) \tag{4b}$$

where

$$\begin{bmatrix} f_X(t) \\ f_Y(t) \end{bmatrix} = \begin{bmatrix} \chi_{0,\mathrm{AC}} \cos\omega t + \chi_{0,X,3\omega} \sin 3\omega t \\ \chi_{0,Y,\omega} \sin\omega t + \chi_{0,Y,3\omega} \sin 3\omega t \end{bmatrix} \tag{5}$$

In (4a) and (4b), terms involving $V_{\mathrm{AC}}{}^2$ have been discarded because the drive voltage is much smaller than the bias voltage in practice, i.e. $V_{\mathrm{AC}}{}^2 \ll V_0{}^2$. The amplitudes of the drive and sense balancing voltage components $V_{X,3\omega}$, $V_{Y,\omega}$, $V_{Y,3\omega}$ are also within the same order of magnitude as V_{AC} since these are also involved in direct forcing of the drive and sense modes. As such, terms involving any product combination of these amplitudes ($V_{\mathrm{AC}}V_{X,3\omega}$, $V_{Y,\omega}V_{X,3\omega}$, $V_{X,3\omega}V_{Y,3\omega}$, $\cdots$) are also neglected. For the same reason, only linear forcing terms involving V_{AC}, $V_{X,3\omega}$, $V_{Y,\omega}$, $V_{Y,3\omega}$ are retained. As such, only the nonlinear electrostatic force from the bias voltage is retained in these equations. The mathematical model accounts for electrostatic nonlinearities up to cubic order, similar to previous studies [4, 19].

X and Y are the drive and sense displacements, and nonlinear electrostatic forces are described by the cubic terms in these modal coordinates (X^3, X^2Y, XY^2, Y^3).

ω_{m} is the mechanical component of the linear resonant frequency, stemming from the total bending potential energy of the ring and support beams.

The electrostatic forces are described by terms involving any combinations of the subscripts '0', '$X, 3\omega$', 'Y, ω', '$Y, 3\omega$' to indicate the contributing voltage components to these terms.

ω_0 is the electrostatic contribution to the linear resonant frequency from the bias voltage. The corresponding terms in (4a) and (4b) are negative, reducing the total linear resonant frequency due to the softening effect of the bias voltage. ω_0 affects the drive and sense modes equally, thus maintaining the linear elastic symmetry between the drive and sense modes. $\omega_0{}^2$ is given by:

$$\omega_0{}^2 = \frac{32\varepsilon_0\delta}{5\rho h\pi {g_0}^3} V_0{}^2 \tag{6}$$

The cubic electrostatic forces are represented by the single and mode-coupled cubic restoring forces with stiffness coefficients γ_0 and κ_0. γ_0 is also known as the modal Duffing coefficient. γ_0 and κ_0 are given by:

$$\gamma_0 = -\frac{16\varepsilon_0}{5\rho h\pi {g_0}^3}\left(3\delta + \frac{\sin 4\delta}{4}\right) V_0{}^2 \tag{7}$$

$$\kappa_0 = -\frac{16\varepsilon_0}{5\rho h\pi {g_0}^3}\left(3\delta - \frac{3\sin 4\delta}{4}\right) V_0{}^2 \tag{8}$$

Since $\gamma_0 < 0$ and $\kappa_0 < 0$, the cubic restoring forces are also of the softening type. γ_0 and κ_0 are coincident when $\delta = \pi/4$, i.e. the case of a continuous electrode. These cubic stiffness coefficients are responsible for the multi-frequency behavior of the drive and sense dynamics if uncompensated.

On the right side of (4a) and (4b), $f_X(t)$ and $f_Y(t)$ are the direct electrostatic forces acting on the drive and sense modes respectively. The 3ω forces $\chi_{0,X,3\omega}\sin 3\omega t$ and $\chi_{0,Y,3\omega}\sin 3\omega t$ in (4a) and (4b) are analogous to balancing force $f_{s,b}(t)$ in (1). $\chi_{0,\mathrm{AC}}$, $\chi_{0,X,3\omega}$, $\chi_{0,Y,\omega}$, $\chi_{0,Y,3\omega}$ are given by:

$$[\chi_{0,\mathrm{AC}} \quad \chi_{0,X,3\omega} \quad \chi_{0,Y,\omega} \quad \chi_{0,Y,3\omega}] = \frac{32\varepsilon_0 \sin\delta}{5\rho h\pi {g_0}^2}[V_0 V_{\mathrm{AC}} \quad V_0 V_{X,3\omega} \quad V_0 V_{Y,\omega} \quad V_0 V_{Y,3\omega}] \tag{9}$$

The bias voltage scales the amplitudes of all these forces. However, in practice, the bias voltage is not directly used for this purpose and is typically used to tune the modal frequencies. As such, in the following, V_{AC}, $V_{X,3\omega}$, $V_{Y,\omega}$, $V_{Y,3\omega}$ are the variables used to control these amplitudes.

4.2. Multi-harmonic balancing

In what follows, the mode-coupled equations of motion are analysed to identify the conditions for the voltage amplitudes V_{AC}, $V_{X,3\omega}$, $V_{Y,\omega}$, $V_{Y,3\omega}$ to reduce or eliminate multi-frequency drive and sense mode vibration responses in a manner similar to the approach discussed in Section 2.

As discussed in Section 2. the multi-frequency behaviour of the drive and sense responses can be expressed as:

$$X = \sum_{m=1}^{m_{max}} \{x_{2m-1}^a \cos[(2m-1)\omega t] - x_{2m-1}^q \sin[(2m-1)\omega t]\} \tag{10a}$$

$$Y = \sum_{m=1}^{m_{max}} \{y_{2m-1}^a \cos[(2m-1)\omega t] - y_{2m-1}^q \sin[(2m-1)\omega t]\} \tag{10b}$$

The amplitudes of the fundamental frequency component ($m = 1$) of the sense response, y_1^a and y_1^q are the quadrature and rate outputs respectively. To solve for the fundamental frequency and the higher harmonic amplitudes $x_{2m-1}^{a,q}$, $y_{2m-1}^{a,q}$, the multiharmonic balancing method [17] can be used. Using this approach, (10a) and (10b) are first substituted into (4a) and (4b), the result of which is multiplied by $\cos(2m-1)\omega t$ and $\sin(2m-1)\omega t$ for each harmonic number m and integrated over the fundamental vibration period $2\pi/\omega$. This process generates $4m_{max}$ simultaneous equations from which $x_{2m-1}^{a,q}$, $y_{2m-1}^{a,q}$ could be solved. However, to determine the voltage conditions to reduce or eliminate multi-frequency response the following approach is adopted.

The targeted single-frequency forms of the drive and sense responses are $X = x^a\cos\omega t - x^q\sin\omega t$ and $Y = y^a\cos\omega t - y^q\sin\omega t$ respectively, where the subscripts have been removed for simplicity (i.e. $x^{a,q} = x_1^{a,q}$ and $y^{a,q} = y_1^{a,q}$). Substituting these expressions into (4a) and (4b) and using the previously described multiharmonic balancing steps up to $m = 2$ gives:

$$\left\{\begin{bmatrix} \boldsymbol{A_{1,XX}}(\omega) & \boldsymbol{A_{1,XY}}(\omega) \\ \boldsymbol{A_{1,YX}}(\omega) & \boldsymbol{A_{1,YY}}(\omega) \end{bmatrix} + \begin{bmatrix} \boldsymbol{A_{3,XX}}(x^a, x^q, y^a, y^q) & \boldsymbol{A_{3.XY}}(x^a, x^q, y^a, y^q) \\ \boldsymbol{A_{3,YX}}(x^a, x^q, y^a, y^q) & \boldsymbol{A_{3,YY}}(x^a, x^q, y^a, y^q) \end{bmatrix}\right\} \boldsymbol{Z} = \boldsymbol{\chi} \tag{11}$$

where $\boldsymbol{\chi}$ is the amplitude vector of the direct force components, given by $\boldsymbol{\chi} = [\chi_{0,\mathrm{AC}} \quad 0 \quad 0 \quad \chi_{0,X,3\omega} \quad 0 \quad \chi_{0,Y,\omega} \quad 0 \quad \chi_{0,Y,3\omega}]^T$. The first 4 rows are associated with drive equation (4a), while the remaining rows are associated with sense equation (4b).

The curly bracketed term is the effective dynamic stiffness matrix, and subscripts '1' and '3' indicate contributions from linear and cubic forces respectively. The partitioned dynamic stiffness matrices are given by:

$$\boldsymbol{A_{1,XX}} = \boldsymbol{A_{1,YY}} = \begin{bmatrix} -\omega^2 + {\omega_m}^2 - {\omega_0}^2 & -2\Gamma\omega \\ -2\Gamma\omega & \omega^2 - {\omega_m}^2 + {\omega_0}^2 \\ 0 & 0 \\ 0 & 0 \end{bmatrix} \tag{12a}$$

$$\boldsymbol{A_{1,XY}} = -\boldsymbol{A_{1,YX}} = \begin{bmatrix} 0 & G_\Omega\Omega\omega \\ G_\Omega\Omega\omega & 0 \\ 0 & 0 \\ 0 & 0 \end{bmatrix} \tag{12b}$$

$$\boldsymbol{A_{3,XX}} = \begin{bmatrix} \frac{3}{4}\gamma_0\frac{{x^a}^2 + {x^q}^2}{{g_0}^2} + \frac{1}{4}\kappa_0\frac{3{y^a}^2 + {y^q}^2}{{g_0}^2} & \frac{1}{2}\kappa_0\frac{y^a y^q}{{g_0}^2} \\ -\frac{1}{2}\kappa_0\frac{y^a y^q}{{g_0}^2} & -\frac{3}{4}\gamma_0\frac{{x^a}^2 + {x^q}^2}{{g_0}^2} - \frac{1}{4}\kappa_0\frac{{y^a}^2 + 3{y^q}^2}{{g_0}^2} \\ \frac{1}{4}\gamma_0\frac{{x^a}^2 - 3{x^q}^2}{{g_0}^2} + \frac{1}{4}\kappa_0\frac{{y^a}^2 - {y^q}^2}{{g_0}^2} & -\frac{1}{2}\kappa_0\frac{y^a y^q}{{g_0}^2} \\ -\frac{1}{2}\kappa_0\frac{y^a y^q}{{g_0}^2} & -\frac{1}{4}\gamma_0\frac{3{x^a}^2 - {x^q}^2}{{g_0}^2} - \frac{1}{4}\kappa_0\frac{{y^a}^2 - {y^q}^2}{{g_0}^2} \end{bmatrix} \tag{12c}$$

$\boldsymbol{A_{3,YY}}$ is identical to $\boldsymbol{A_{3,XX}}$ with x^a, x^q interchanged with y^a, y^q. $\boldsymbol{A_{3,YX}}$ and $\boldsymbol{A_{3,XY}}$ are zero matrices.

$\boldsymbol{Z}$ is a vector containing the fundamental frequency displacement amplitudes, given by $\boldsymbol{Z} = [x^a \quad x^q \quad y^a \quad y^q]^T$. For an ideal, linear device:

$$\boldsymbol{Z} = \boldsymbol{Z_t} = \left[0 \quad -x \quad 0 \quad \frac{G_\Omega\Omega}{2\Gamma}x\right]^T \tag{13}$$

where $\boldsymbol{Z_t}$ is the targeted form of the amplitude vector. For this case, $x^a = 0$ and $x^q = -x$ because the drive response is resonant with amplitude x. For the sense response, $y^a = 0$, indicating a zero quadrature response relative to the drive mode, and $y^q = G_\Omega\Omega x/(2\Gamma)$, indicating that the rate output scales proportionally with drive amplitude.

To ensure $\boldsymbol{Z} = \boldsymbol{Z_t}$ is the solution to (11) so as to recover ideal, linear, single-frequency drive and sense responses, $\boldsymbol{Z} = \boldsymbol{Z_t}$ is substituted into (11) and the resulting equation solved for $\chi_{0,X,3\omega}$, $\chi_{0,Y,\omega}$ and $\chi_{0,Y,3\omega}$. Following this procedure the necessary frequency and force conditions are:

$$\omega^2 = {\omega_X}^2 = {\omega_m}^2 - {\omega_0}^2 + \frac{3}{4}\gamma_0\frac{x^2}{{g_0}^2} + \frac{3}{4}\kappa_0\frac{y^2}{{g_0}^2} \tag{14a}$$

$$\chi_{0,X,3\omega}|_t = -\frac{1}{4}x\left(\gamma_0\frac{x^2}{{g_0}^2} + \kappa_0\frac{y^2}{{g_0}^2}\right) \tag{14b}$$

$$\chi_{0,Y,\omega}|_t = \left(\omega^2 - {\omega_m}^2 + {\omega_0}^2 - \frac{3}{4}\gamma_0\frac{y^2}{{g_0}^2} - \frac{3}{4}\kappa_0\frac{x^2}{{g_0}^2}\right)\frac{G_\Omega\Omega}{2\Gamma}x \tag{14c}$$

$$\chi_{0,Y,3\omega}|_t = \frac{1}{4}\left(\gamma_0\frac{y^2}{{g_0}^2} + \kappa_0\frac{x^2}{{g_0}^2}\right)\frac{G_\Omega\Omega}{2\Gamma}x \tag{14d}$$

where $y = G_\Omega|\Omega|x/(2\Gamma)$ is the sense amplitude.

In (14a), ω_X is the resonant drive frequency. Noting from (7) and (8) that γ_0 and κ_0 are negative, the drive frequency decreases with the drive and sense amplitude, indicating a nonlinear softening behaviour. In previous analyses [4, 19], the term involving y^2 is typically discarded as the sense-to-drive back coupling is neglected. In practice, the PLL is used to set $\omega = \omega_X$.

In (14b) and (14d), the presence of the cubic stiffness coefficients γ_0, κ_0 necessitates the presence of 3ω drive and sense balancing forces to negate the multi-frequency behaviour. It's worth noting that the required 3ω balancing force amplitudes $\chi_{0,X,3\omega}|_t$ and $\chi_{0,Y,3\omega}|_t$ increase with drive amplitude such that

$\chi_{0,X,3\omega}|_t \propto x^3$ and $\chi_{0,Y,3\omega}|_t \propto x^3$. In practice, control loops are required to ensure that the 3ω balancing force amplitudes satisfies force conditions in (14b) and (14d). This can be achieved by tracking the 3ω drive and sense response components simultaneously, and adjusting $\chi_{0,X,3\omega}$ and $\chi_{0,Y,3\omega}$ until the 3ω response components nullify. These implementations will be demonstrated later. To nullify the 3ω sense response, the required balancing force amplitude $\chi_{0,Y,3\omega}|_t$ is proportional to the angular rate.

Satisfying (14c) ensures quadrature output is nullified. The bracketed term is the nonlinear frequency imbalance, which is a nonlinear extension of the linear frequency split. When the drive mode is resonant ((14a)), $\chi_{0,Y,\omega}|_t = 0$ if $\gamma_0 = \kappa_0$ and occurs for the continuous electrode arrangement, i.e. $\delta = \pi/4$ (see (7) and (8)). In this case the quadrature output is naturally zero due to the absence of nonlinear frequency imbalance and the 1ω sense balancing voltage component is not required and $V_{Y,\omega}$ can be set to zero.

Noting the definitions of the balancing force amplitudes $\chi_{0,X,3\omega}$, $\chi_{0,Y,\omega}$, $\chi_{0,Y,3\omega}$ in (9), the balancing force amplitude conditions in (14b) – (14d) give the voltage conditions for $V_{X,3\omega}$, $V_{Y,\omega}$, $V_{Y,3\omega}$ to achieve the targeted single-frequency drive and sense response.

5. Results

In this section, the effectiveness of applying 3ω balancing voltage components to achieve linear, single-frequency drive and sense vibration is investigated. The frequency stabilising effects of the implementation are assessed using numerical results for the Allan deviation of the rate output, where the higher harmonic drive and sense response components are treated as pseudo-noise sources.

The following results are based on the system parameters and operating conditions listed in Table 1.

Table 1. Parameters and operating conditions

Symbol	Value
ρ (kg/m^3)	2320
R (μm)	550
h (μm)	4
g_0 (μm)	1.4
ω_m (kHz)	13.5
Γ (Hz)	56.4
Ω (°/s)	250
δ (°)	38
V_0 (V)	2.1

Voltage components (V_AC, $V_{X,3\omega}$, $V_{Y,\omega}$, $V_{Y,3\omega}$) are varied depending on the cases investigated.

FE results are also included to validate the effectiveness of the proposed approach. These results are obtained using a transient study of an electrostatic model in COMSOL. A time history of the radial ring displacement is obtained at multiple evenly-spaced points on the ring centerline, which are then used to conduct a circumferential Fourier decomposition to determine the 2θ circumferential variation components of radial displacement at each time step at steady state. These components are used to extract time histories for the steady-state drive X and sense displacements Y.

5.1. Modal amplitude spectra

To demonstrate the influence of balancing voltage on the multi-frequency behaviour of the drive and sense vibration, the FFT of the steady-state drive and sense displacements is considered, with comparisons made between the default unbalanced case ($V_{X,3\omega} = V_{Y,\omega} = V_{Y,3\omega} = 0$) and with the conditions (14b) – (14d) satisfied.

The effects of the 3ω balancing voltage components on the 3ω drive and sense response components are first investigated. Equations of motion (4a) and (4b) are solved to obtain the time histories of the drive and sense displacements until steady-state is achieved. Based on the steady-state drive and sense displacements, Figure 3(a) and (b) show the amplitudes of the 3ω drive and sense displacement

components as the 3ω drive and sense balancing voltage amplitudes are varied up to twice the required values to satisfy (14b) and (14d), which are $V_{X,3\omega}|_t = 0.92\ mV$ and $V_{Y,3\omega}|_t = -7.12\ \mu V$ respectively. In these results, the drive amplitude is fixed at 10% of the capacitive gap, requiring a drive voltage amplitude of $V_{\mathrm{AC}} = 5.5\ mV$, and the driving frequency is fixed at the drive resonant frequency ω_X (condition in (14a)) at 11.4 kHz. The required 1ω sense balancing voltage amplitude $V_{Y,\omega}$ to eliminate the quadrature output y^a is $V_{Y,\omega}|_t = -6\ \mu V$ (condition in (14c)). FE results are also included at the data points near $V_{X,3\omega} = V_{X,3\omega}|_t$ and $V_{Y,3\omega} = V_{Y,3\omega}|_t$.

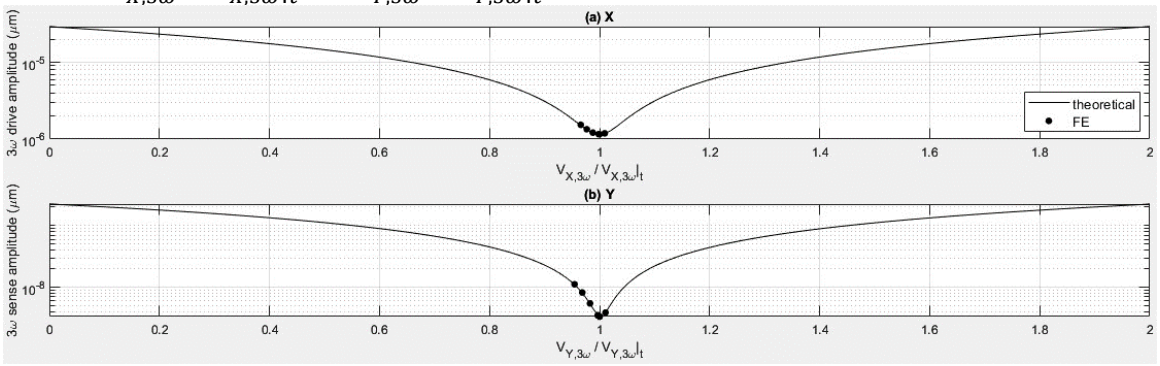

Figure 3. Effects of the 3ω (a) drive and (b) sense balancing voltage amplitudes on the 3ω drive and sense vibration amplitude components respectively.

Both the 3ω drive and sense amplitude components minimise when $V_{X,3\omega} = V_{X,3\omega}|_t$ and $V_{Y,3\omega} = V_{Y,3\omega}|_t$, and the FE results are in good agreement with the theoretical results. These results indicate that the minimisation of the 3ω drive and sense amplitude components offers a practical means to determine the required 3ω balancing voltage amplitudes $V_{X,3\omega}|_t$ and $V_{Y,3\omega}|_t$.

Figure 4(a) and (b) show the FE results for the drive and sense amplitude spectra for the cases where no 3ω balancing voltages are applied ($V_{X,3\omega} = V_{\mathrm{Y},3\omega} = 0$) and with the 3ω balancing voltages applied to satisfy (14b) and (14d), i.e. $V_{\mathrm{X},3\omega} = V_{\mathrm{X},3\omega}|_t, V_{\mathrm{Y},3\omega} = V_{\mathrm{Y},3\omega}|_t$. In both sets of results, the FE transient studies are run for 900 load cycles to ensure sufficient decay of the transient response to obtain the 3ω drive and sense amplitude components with sufficient accuracy. The number of load cycles chosen is limited due to the significant computation time involved to obtain the time histories of the drive and sense displacements, which is within the order of days.

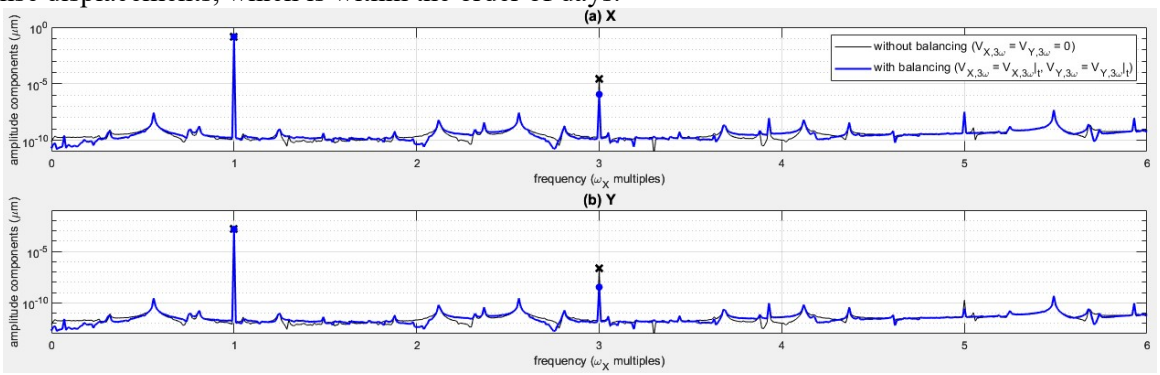

Figure 4. Comparison of (a) drive and (b) sense amplitude spectra for the 3ω-unbalanced ($V_{X,3\omega} = V_{Y,3\omega} = 0$) and balanced ($V_{X,3\omega} = V_{X,3\omega}|_t, V_{Y,3\omega} = V_{Y,3\omega}|_t$) cases.

The drive and sense displacements exhibit amplitude components at the fundamental frequency ω and 3ω. The amplitude peaks for the higher harmonics (5ω, 7ω, 9ω, $\cdots$) are not revealed as the transient response is not sufficiently attenuated with the chosen number of load cycles.

The amplitudes of the fundamental frequency component of the drive and sense displacements are unaffected by the presence of the 3ω balancing voltages. However, the 3ω drive and sense amplitude

components reduce by 2 orders of magnitude when the 3ω balancing voltages are applied. The multi-frequency behaviour is not fully negated as the FE model also includes higher order electrostatic nonlinearities (beyond cubic) which are not accounted for in the present theoretical analysis. Additionally, all nonlinear forces involving the direct forcing voltage amplitudes $V_{AC}, V_{X,3\omega}, V_{Y,\omega}, V_{Y,3\omega}$ have been discarded from (4a) and (4b). However, the reduced 3ω drive and sense amplitude components confirm that the proposed direct approach suppresses the multi-frequency behaviour.

5.2. Rate readout and Allan deviation

The device rate readout of the device is now considered, which is determined from the multi-frequency sense displacement. The higher harmonic drive and sense components are treated as pseudo-noise sources distorting the rate readout, and the effects on the Allan deviation of the rate readout are investigated.

The rate readout Ω_{out} is determined from sense displacement Y. Provided the drive mode is resonant ($\omega = \omega_X$) and the 1ω sense balancing voltage has been set to negate the quadrature output (condition (14c)), the rate readout is defined as:

$$\Omega_{out}(t) = \frac{1}{S}\left[2Y\sin\omega_X t + \left(\frac{\omega_X}{2\pi}\int_0^{2\pi/\omega_X} 2Y\sin\omega_X t\,dt\right)\cos 2\omega_X t\right]$$

where $S = G_\Omega x/(2\Gamma)$ is the scale factor (see definition of rate output y^q in (13)).

In the bracketed term, $\sin\omega_X t$ represents the drive phase as it oscillates at a $-\pi/2$ phase lag relative to the harmonic drive force $\chi_{0,\mathrm{AC}}\cos\omega t$. The multiplication of the sense displacement signal Y with $\sin\omega_X t$ is commonly implemented in the demodulation process to obtain the rate readout as the drive vibration phase is used as the demodulation reference [11, 12]. The fundamental frequency component in the sense displacement also generates a $2\omega_X$ signal after the multiplication $Y\sin\omega_X t$, so the second term involving the integral is aimed at negating this $2\omega_X$ signal. As such, in the linear, ideal case where the sense displacement has a single frequency ($Y = -y^q\sin\omega t$), the rate readout is constant and equal to the angular rate input, i.e. $\Omega_{out} = \Omega$. As such, any time variation of the rate readout is directly attributed to the presence of higher harmonics in the sense displacement.

Figure 5 shows the FE results for the rate readout error for the cases without the 3ω balancing voltages ($V_{X,3\omega} = V_{Y,3\omega} = 0$) and with the 3ω balancing voltages applied i.e. $V_{X,3\omega} = V_{X,3\omega}|_t, V_{Y,3\omega} = V_{Y,3\omega}|_t$. In the plot, the final 10 load cycles of the FE transient study have been used to ensure the transient response effects are minimised.

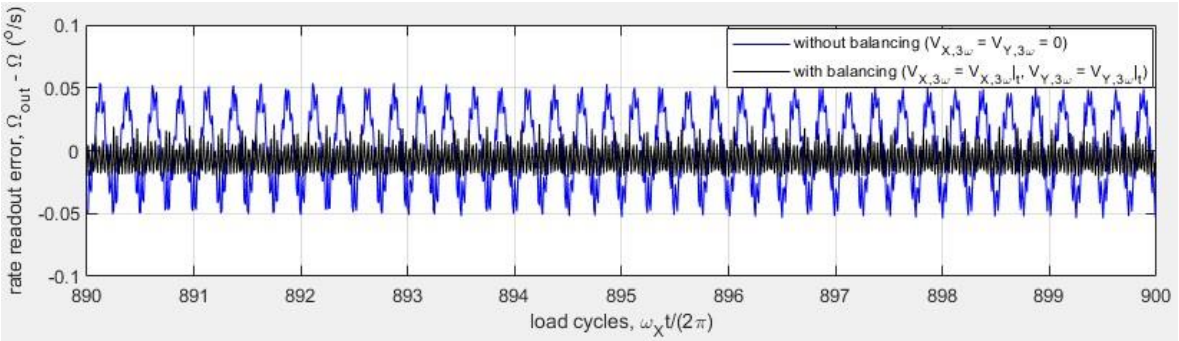

Figure 5. Time histories of rate readout errors for the 3ω-unbalanced ($V_{X,3\omega} = V_{Y,3\omega} = 0$) and balanced ($V_{X,3\omega} = V_{X,3\omega}|_t, V_{Y,3\omega} = V_{Y,3\omega}|_t$) cases.

The 3ω balancing voltage significantly reduces the rate readout error. This is due to the reduced 3ω sense amplitude component, as shown in Figure 4(b). The magnitude of the rate readout fluctuation is comparable with typical MEMS gyroscopes [12], indicating that these deterministic nonlinearities have non-negligible impact on rate readout compared to random noise sources.

The rate readout without 3ω balancing voltages exhibits periodicity, where the dominant frequency component is 4ω stemming from the 3ω and 5ω sense amplitude components. This periodicity is the direct result of the higher harmonics within the sense displacement. The 4ω rate readout periodicity is not clearly shown for the case with the 3ω balancing voltages applied because the 3ω sense displacement amplitude has been reduced significantly such that it is only 1 order of magnitude larger than the transient response, as shown in Figure 4(b).

Figure 6 shows the Allan deviation of the rate readout for the same systems used in Figure 5. Similar to the results in Figure 5, only the last 10 load cycles of the rate readout time history is considered when calculating the Allan deviation results, limiting the averaging time to 0.43 ms.

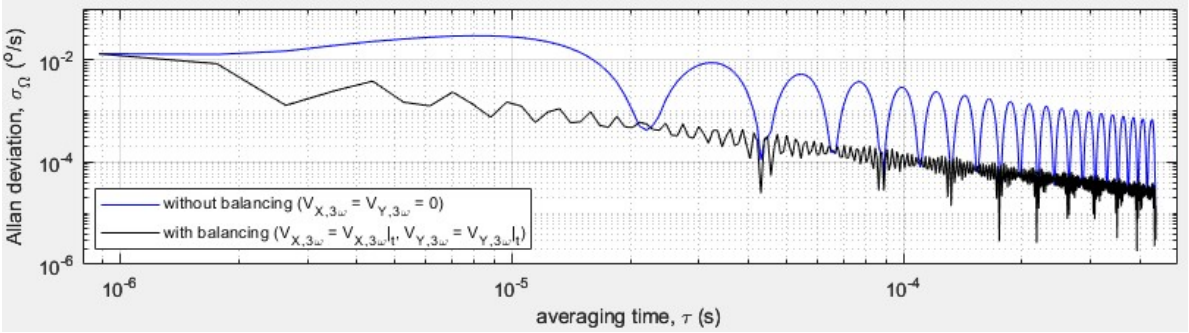

Figure 6. Allan deviation of rate readout comparison between the 3ω-unbalanced ($V_{X,3\omega} = V_{Y,3\omega} = 0$) and balanced ($V_{X,3\omega} = V_{X,3\omega}|_t, V_{Y,3\omega} = V_{Y,3\omega}|_t$) cases.

Applying the 3ω balancing voltage reduces the Allan deviation by 1 order of magnitude, indicating improved frequency stability of the rate readout. The achieved reduction is limited by the strength of higher order electrostatic nonlinearities, which are not compensated for using the proposed approach.

6. Conclusion

An approach using electrostatic forces to suppress the multi-frequency mechanical vibrations in MEMS ring-based CVG's has been investigated. The approach involves applying direct electrostatic forces on the drive and sense modes to counterbalance residual higher frequency forces caused by electrostatic nonlinearities, up to cubic order. It is found that specific conditions must be satisfied to achieve this balancing, necessitating the use of harmonic drive and sense balancing voltages at triple the drive frequency.

The proposed implementation is shown to reduce the higher harmonic drive and sense response components by orders of magnitude. This results in improved frequency stability as indicated by lower Allan deviations, and reduced device rate readout fluctuations. The attainable frequency stability improvement is limited by the presence of higher order electrostatic nonlinearities. However, the proposed approach can be extended to account for these higher order electrostatic nonlinearities.

References

[1] C. Acar and A. Shkel, *MEMS Vibratory Gyroscopes-Structural Approaches to Improve Robustness*, 1 ed. Springer US, 2009.

[2] J. Sun, S. Yu, Y. Zhang, Q. Li, X. Xi, K. Lu, X. Wu, and D. Xiao, "0.79 ppm scale-factor nonlinearity whole-angle microshell gyroscope realized by real-time calibration of capacitive displacement detection," *Microsystems & Nanoengineering,* vol. 7, no. 1, p. 79, 2021/10/13 2021.

[3] S. Timoshenko, *Vibration problems in engineering*, 5 ed. New York: Wiley, 1990.

[4] D. Arifin and S. McWilliam, "Effects of electrostatic nonlinearity on the rate measuring performance of ring based Coriolis Vibrating Gyroscopes (CVGs)," *Sensors and Actuators A: Physical,* vol. 340, p. 113539, 2022/06/16/ 2022.

[5] B. Chouvion, S. McWilliam, and A. A. Popov, "Effect of nonlinear electrostatic forces on the dynamic behaviour of a capacitive ring-based Coriolis Vibrating Gyroscope under severe shock," *Mechanical Systems and Signal Processing,* vol. 106, pp. 395-412, 2018/06/01/ 2018.
[6] D. Vatanparvar and A. M. Shkel, "Instabilities due to Electrostatic Tuning of Frequency-Split in Coriolis Vibratory Gyroscopes," in *2020 IEEE SENSORS*, 2020, pp. 1-4.
[7] G. Sérandour, "Non-linear dynamics of vibratory rate sensors," PhD, University of Nottingham, 2005.
[8] L. Huang, S. M. Soskin, I. A. Khovanov, R. Mannella, K. Ninios, and H. B. Chan, "Frequency stabilization and noise-induced spectral narrowing in resonators with zero dispersion," *Nature Communications,* vol. 10, no. 1, p. 3930, 2019/09/02 2019.
[9] H. K. Lee, P. A. Ward, A. E. Duwel, J. C. Salvia, Y. Q. Qu, R. Melamud, S. A. Chandorkar, M. A. Hopcroft, B. Kim, and T. W. Kenny, "Verification of the phase-noise model for MEMS oscillators operating in the nonlinear regime," in *2011 16th International Solid-State Sensors, Actuators and Microsystems Conference*, 2011, pp. 510-513.
[10] N. Miller, "Noise in nonlinear micro-resonators," PhD, Michigan State University, 2012.
[11] D. Vatanparvar and A. M. Shkel, "Quadrature-Induced Noise in Coriolis Vibratory Gyroscopes," in *2020 IEEE International Symposium on Inertial Sensors and Systems (INERTIAL)*, 2020, pp. 1-4.
[12] X. Ding, J. Jia, Y. Gao, and H. Li, "Mechanical and Electrical Noise in Sense Channel of MEMS Vibratory Gyroscopes," *Sensors*, vol. 17, no. 10. doi: 10.3390/s17102306
[13] D. Antonio, D. H. Zanette, and D. López, "Frequency stabilization in nonlinear micromechanical oscillators," (in English), *Nature Communications,* vol. 3, p. 806, 2012.
[14] M. Agarwal, S. A. Chandorkar, R. N. Candler, B. Kim, M. A. Hopcroft, R. Melamud, C. M. Jha, T. W. Kenny, and B. Murmann, "Optimal drive condition for nonlinearity reduction in electrostatic microresonators," *Applied Physics Letters,* vol. 89, no. 21, p. 214105, 2006.
[15] B. Yurke, D. S. Greywall, A. N. Pargellis, and P. A. Busch, "Theory of amplifier-noise evasion in an oscillator employing a nonlinear resonator," *Physical Review A,* vol. 51, no. 5, pp. 4211-4229, 05/01/ 1995.
[16] B. Sun, C. Zhao, G. Sobreviela-Falces, S. Du, F. Han, X. Zou, and A. Seshia, "Enhanced frequency stability in a non-linear MEMS oscillator employing phase feedback," in *2017 IEEE 30th International Conference on Micro Electro Mechanical Systems (MEMS)*, 2017, pp. 1115-1117.
[17] E. P. Petrov and D. J. Ewins, "State-of-the-art dynamic analysis for non-linear gas turbine structures," (in English), *Proceedings of the Institution of Mechanical Engineers,* vol. 218, no. 3, pp. 199-211, 2004.
[18] A. Cardona, T. Coune, A. Lerusse, and M. Geradin, "A multiharmonic method for non-linear vibration analysis," *International Journal for Numerical Methods in Engineering,* vol. 37, no. 9, pp. 1593-1608, 1994/05/15 1994.
[19] P. M. Polunin and S. W. Shaw, "Self-induced parametric amplification in ring resonating gyroscopes," *International Journal of Non-Linear Mechanics,* vol. 94, pp. 300-308, 2017/09/01/ 2017.
[20] H. Cao, Y. Liu, Z. Kou, Y. Zhang, X. Shao, J. Gao, K. Huang, Y. Shi, J. Tang, C. Shen, and J. Liu, "Design, Fabrication and Experiment of Double U-Beam MEMS Vibration Ring Gyroscope," *Micromachines,* vol. 10, no. 3, 2019.
[21] B. J. Gallacher and J. S. Burdess, "Dynamic analysis of a microelectromechanical systems resonant gyroscope excited using combination parametric resonance," *Proceedings of the Institution of Mechanical Engineers. Part C, Journal of mechanical engineering science,* vol. 220, no. 9, pp. 1463-1479, 2006.
[22] D. Arifin, "Using electrostatic nonlinearities to enhance the performance of ring-based Coriolis vibratory gyroscopes," PhD, University of Nottingham, 2023.